Multisite Downscaling of Seasonal Predictions to Daily Rainfall Characteristics over Pacific–Andean River Basins in Ecuador and Peru Using a Nonhomogeneous Hidden Markov Model

LUIS E. PINEDA

Hydraulics Division, Department of Civil Engineering, Katholieke Universiteit Leuven, Leuven, Belgium, and Departamento de Geología, Minas e Ingeniería Civil, Universidad Técnica Particular de Loja, San Cayetano, Loja, Ecuador

PATRICK WILLEMS

Hydraulics Division, Department of Civil Engineering, Katholieke Universiteit Leuven, Leuven, Belgium

(Manuscript received 20 March 2015, in final form 29 September 2015)

ABSTRACT

The seasonal predictability of daily rainfall characteristics is examined over 21 hydrologic units in the Pacific–Andean region of Ecuador and Peru (PAEP) using a nonhomogeneous hidden Markov model (NHMM) and retrospective seasonal information from general circulation models (GCMs). First, a hidden Markov model is used to diagnose four states that play distinct roles in the December–May rainy season. The estimated daily states fall into two wet states, one dry state, and one transitional dry–wet state, and show a systematic seasonal evolution together with intraseasonal and interannual variability. The first wet state represents regionwide wet conditions, while the second one represents north–south gradients. The former could be associated with the annual moisture offshore of the PAEP, thermally driven by the climatological maximum of sea surface temperatures in the Niño-1.2 region. The latter corresponds with the dynamically noisy component of the PAEP rainfall signal, associated with the annual displacement of the intertropical convergence zone. Then, a four-state NHMM is coupled with GCM information to simulate daily sequences at each station. Simulations of the GCM–NHMM approach represent daily rainfall characteristics at station level well. The best skills were found in reproducing the interannual variation of seasonal rainfall amount and mean intensity at the regional-averaged level with correlations equal to 0.60 and 0.64, respectively. At catchment level, the best skills appear over catchments south of 4°S, where hydrologically relevant characteristics are well simulated. It is thus shown that the GCM–NHMM approach provides the potential to produce precipitation information relevant for hydrological prediction in this climate-sensitive region.

1. Introduction

Because of its meteorological and societal impacts, predictions of the seasonal to daily characteristics of the rainy season are crucial to climate-sensitive regions; many management decisions in agriculture, water, and disaster reduction fall into the subseasonal to seasonal time range. The December–May rainy season in the Pacific–Andean region of Ecuador and Peru (PAEP) contributes about 75%–90% of the annual precipitation total (Rossel and Cadier 2009) and is essential to sustain crop production. In fact, more than 68% of the Ecuadorian crop production originates from lowland irrigated basins in the central Ecuadorian coast (Borbor-Cordova et al. 2006). Precipitation is also important for agriculture and settlements on nonirrigated valleys west of the Andes, where the December–May distribution of precipitation determines the existence of vegetation cycles (Emck 2007). Water economics, food security, and disaster preparedness, among other related sectors in the PAEP, require daily within-season rainfall predictions to derive climate risk management strategies.

December–May rainfall in the PAEP is also known for its year-to-year variability driven by El Niño–Southern

Denotes Open Access content.

Corresponding author address: L. E. Pineda, Hydraulics Division, Department of Civil Engineering, Katholieke Universiteit Leuven, Kasteelpark Arenberg 40, BE-3001 Leuven, Belgium.
E-mail: pineda.luis40@gmail.com

DOI: 10.1175/JHM-D-15-0040.1

Oscillation (ENSO). ENSO episodes are generally associated with an enhancement of the December–May rainfall productivity, particularly observed during the strongest ENSO events (i.e., 1982/83 and 1997/98) (Bendix 2000; Vuille et al. 2000; Takahashi 2004), concomitant with the maxima of sea surface temperature (SST) anomalies over the eastern equatorial Pacific. Related to the influence of SSTs on the December–May rainfall variability, some of the highest skills from current dynamical climate models occur while detecting SST anomalous patterns over the equatorial Pacific (Barnston et al. 1999). Yet, the associated skill of the dynamical seasonal prediction models (e.g., Goddard et al. 2003) and their statistical correction (Recalde-Coronel et al. 2014) has not been assessed for the December–May daily rainfall over this region. Therefore, an emerging question is whether such skillful seasonal forecasts can be translated into regionwide predictions of daily rainfall statistics, which, if anticipated with a useful lead time, can be used to warn the likelihood of high-impact weather (floods and droughts) by extending hydrological forecasting with rainfall–runoff hydraulic models to longer times.

In the PAEP, traditional approaches to seasonal hydroclimatic forecasting have only relied on observations of hydrological conditions, that is, seasonal reservoir inflows are usually estimated based on antecedent streamflow conditions. Upcoming-season hydrological conditions, however, also rely on the upcoming climate conditions, which are subject to year-to-year fluctuations (Rossel and Cadier 2009). Hence, the incorporation of seasonal climate predictions becomes important for hydrologic prediction tools. Hydroclimatic seasonal forecasting has just received attention and is still an area of emerging research for the National Meteorological and Hydrological Services (NMHS; Recalde-Coronel et al. 2014). On the way to hydrological prediction, targeted to local users, the main challenges for the NMHS are 1) the lack of accurate high-resolution seasonal forecasts from general circulation models (GCMs) and 2) the institutional barriers to cope with this lack of information and turn it into readily available products for water resource needs. Although efforts have been made to set up regional climate models (RCMs; i.e., Muñoz et al. 2010), RCM reanalysis still shows modest skills in representing daily to seasonal precipitation over this region (Ochoa et al. 2014). Accordingly, the coarse seasonal prediction of precipitation made with GCMs continues to be the most comprehensive quantitative characterization of the regional climate. Unfortunately, the spatial scale at which this information is available does not represent the characteristics of local daily rainfall. This limits its applicability for direct intake in hydrological prediction models.

We propose a nonhomogeneous hidden Markov model (NHMM; Hughes and Guttorp 1994; Robertson et al. 2004) as a simple method to capture the statistics of multisite daily precipitation data and link them to GCM information. The NHMM decomposes the observed spatiotemporal rainfall variability over a set of rain gauge stations by means of a small set of daily weather patterns (discrete ''hidden'' states). Each state consists of a set of wet-day probabilities and rainfall distributions for the entire network. The nonhomogeneous feature allows transition probabilities to vary between states, allowing external inputs (GCM-based information) to influence rainfall characteristics. In benchmark exercises, seasonal GCM precipitation predictions have been used as inputs, creating an effective way to downscale the most probable daily rainfall sequences over a network of stations (Robertson et al. 2004, 2006, 2009; Verbist et al. 2010). Yet, this probabilistic modeling framework has not been applied to examine the predictability of the December–May daily rainfall in the PAEP. Here, we assess the ability of a GCM–NHMM framework to downscale seasonal climate predictions from GCMs to multisite daily precipitation characteristics over this region.

We consider a discrete weather state decomposition an adequate method to model daily rainfall characteristics in an information-scarce region such as PAEP. The use of the hidden Markov model (HMM) as a diagnostic tool for the characterization of the regional climate fits well in this region, where literature regarding weather types simply does not exist. This makes the present work novel regarding the diagnostic utility of the HMM to characterize rainfall states in terms of persistent weather patterns in this region. We apply and build the GCM–NHMM framework in two steps. First, we use the HMM to identify states and relationships between each state and large-scale modes of ocean–atmosphere forcing. By doing so, we seek to establish the physical basis for the predictability of a network of 68 daily rainfall stations over 21 catchments. In the second step, we identify levels and sources of predictability for the December–May rainy season from two GCMs, then we train the NHMM on each year for which skillful seasonal predictors were identified and use it to hindcast December–May daily rainfall in the PAEP relevant for catchment hydrology.

2. Study area and data

a. *PAEP and climate*

The PAEP ($\sim$100 800 km^2) is located along the north–south axis between 0° and 6°S and drains the westernmost slope of the Andes (Fig. 1). The seasonal rainfall

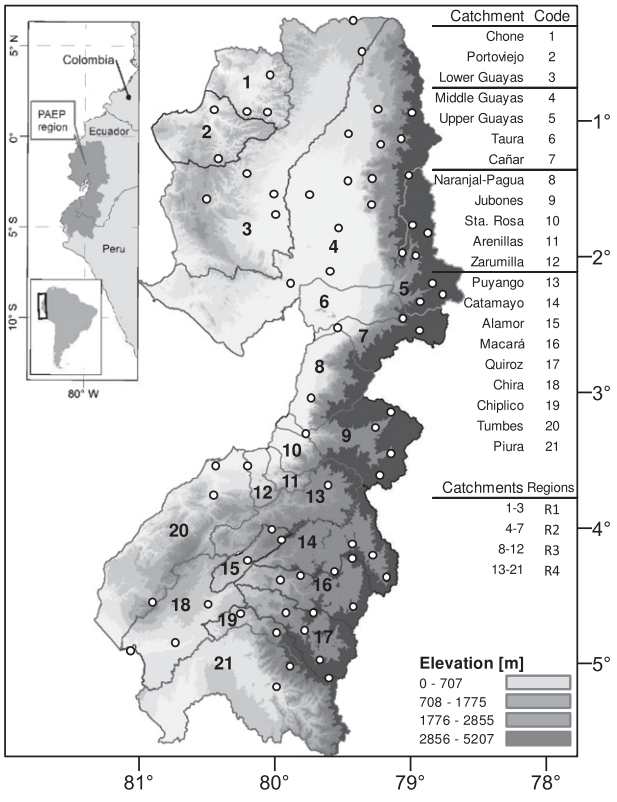

FIG. 1. Topography (shaded in gray) and catchments (dark gray line) in the PAEP with rain gauge stations (white dots). Location of the study area in northwestern South America is shown in the inset.

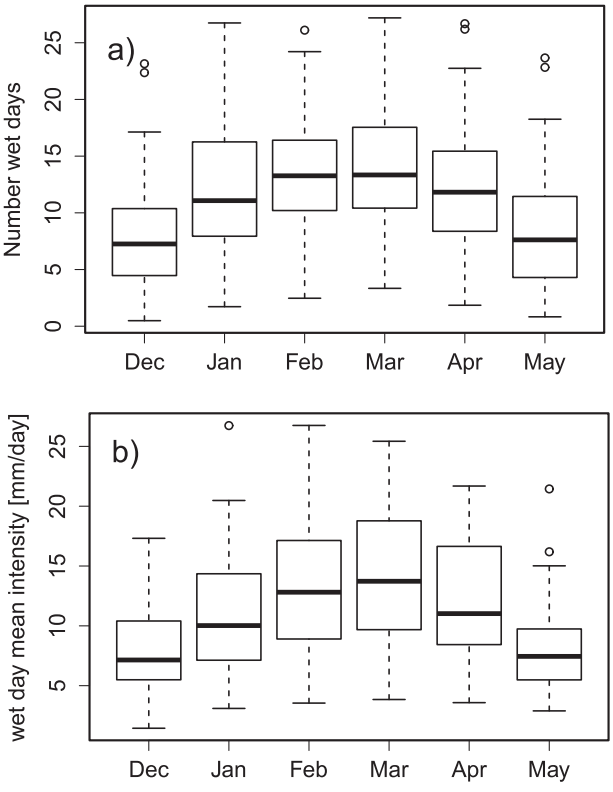

FIG. 2. Box-and-whisker plots of the daily rainfall characteristics for December–May in the PAEP. (a) Number of wet days (≥0.1 mm) and (b) rainfall intensity (mm day^{-1}) on wet days. The whiskers extend to the 1.5 interquartile range. Dots show outlying values.

distribution in the PAEP is characterized by a single rainy period, with 75%–90% of the rainfall occurring between December and May. The (December–May) rainy season is mainly influenced by the seasonal latitudinal migration of the intertropical convergence zone (ITCZ) and eastern tropical Pacific SST variations. The north–south seasonal ITCZ displacement and SST variations bring air masses of different humidity and temperature to the area (Rossel and Cadier 2009). The western Andes and coastal ridges descend down to the coast, shaping a series of intersecting valleys with different exposure to oceanic–atmospheric moisture. This results in a patchy spatial rainfall structure with horizontal gradients down to the coast and a vertical increase of precipitation elsewhere (Emck 2007). This study focuses on 21 homogeneous hydrological units (catchments 1–21 in Fig. 1) identified by Ochoa et al. (2014) and located in four hydroclimate regions in the PAEP. Regions represent catchments in different climate zones: humid northern and coastal catchments (R1); humid northern inner-Andean valleys (R2); central short, steep catchments (R3); and southern catchments in the transition to arid conditions in northern Peru (R4).

b. *Rainfall data*

A 46-yr record of December–May daily rainfall (8372 days) at 68 stations was extracted from an extensive and quality-controlled dataset of daily series (107) available for 1964–2010. The selected stations have the most complete and reliable records. This dataset has been comprehensively evaluated, ensuring temporal homogeneity in each record (Ochoa et al. 2014). The raw data were provided by both the Ecuadorian and Peruvian NMHS [Instituto Nacional de Meteorología e Hidrología (INAMHI) and Servicio Nacional de Meteorología e Hidrología (SENAMHI), respectively].

Figure 2 shows the climatological values of daily rainfall occurrences and mean intensity of rainfall on wet days (>1 mm) within December–May. Seasonality modulates both rainfall frequency and intensity. The peak centers within February–March and is more pronounced for mean intensity. Figure 3 shows the spatial distribution of seasonal totals, wet-day probabilities, and mean wet-day rainfall intensities together with the 21 homogenous units. Rainfall characteristics are more homogenous over catchments north of 3°S. The highest

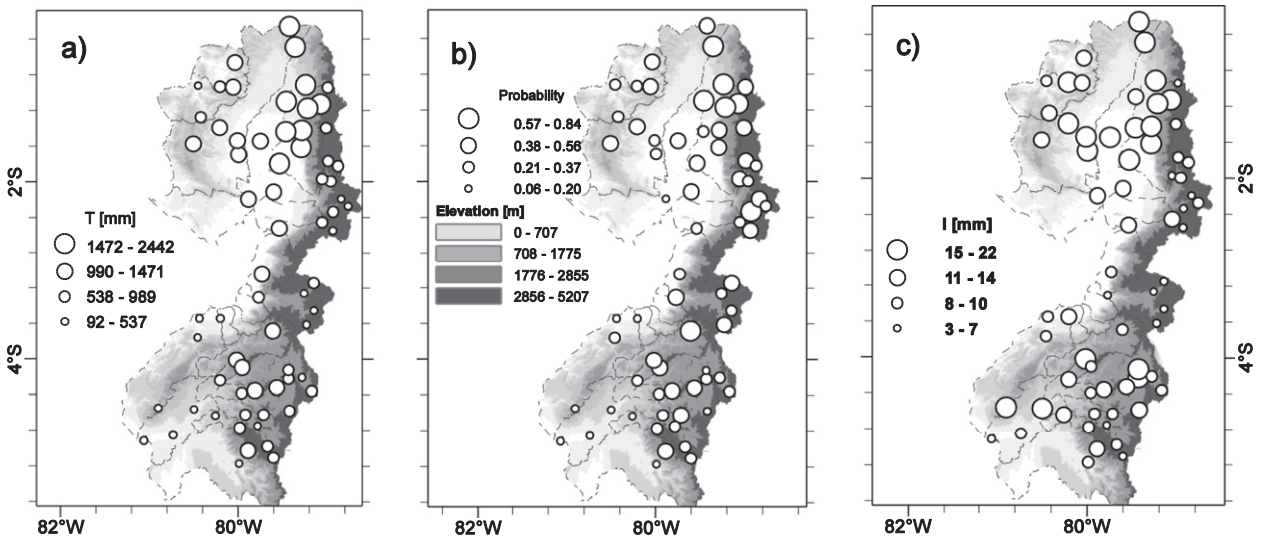

FIG. 3. Regional daily rainfall characteristics during the rainy season (December–May). (a) Seasonal rainfall amount, (b) wet-day probability, and (c) mean wet-day intensity for 1964–2010.

probabilities and mean daily intensities occur in the Middle Guayas (4) while the lowest occur over the southwestern edge at Tumbes (20), Chira (18), and Piura (21), a transition zone toward more arid conditions in northern Peru. The complex terrain structure plays a major role south of 3°S, where the more scattered distribution of probabilities and mean intensities reflect windward and leeward effects of the southern Andes on the spatial distribution of rainfall.

c. *GCM seasonal forecast models and SST data*

Retrospective seasonal December–May precipitation forecasts initialized on 1 November were obtained from two GCMs: ECHAM4.5 (Roeckner et al. 1996) and the National Centers for Environmental Prediction (NCEP) Climate Forecast System, version 2 (CFSv2; Saha et al. 2006, 2014). ECHAM is an atmospheric GCM that is driven with the same constructed analog (CA) predictions of global SST in a two-tiered approach (Li and Goddard 2005). This approach has been used as the basis of the International Research Institute for Climate and Society (IRI) operational seasonal forecast system since 1997 (Barnston et al. 2010). Historical ECHAM4.5 simulations in which ECHAM4.5 is driven by observed SSTs are also used in this study. We refer to the former as ECHAM4.5ca and to the latter as ECHAM4.5hi. CFSv2 is a coupled ocean–atmosphere GCM with initialization of the atmosphere, ocean, and land surface conditions through data assimilation. For ease of comparison, the ensemble-mean (over 24 members for ECHAM and 28 members for CFSv2) gridded monthly precipitation was used at a resolution of T62 (~1.9°) for CFSv2 and T42 (~2.8°) for ECHAM4.5ca, over the domain 15°N–15°S and 65°–100°W. We also make use of predicted CFSv2 SSTs and gridded monthly Extended Reconstructed SST, version 3 (ERSSTv3; Smith et al. 2008) extracted from the National Oceanic and Atmospheric Administration/National Climatic Data Center (NOAA/NCDC) archives. This 2° latitude–longitude dataset is a global merged land, air, and SST reconstruction based on historical observations.

3. Methods

a. *The HMM structure and assumptions*

We first use the homogenous HMM version as a diagnostic tool to provide a compact description of the December–May daily rainfall variability and its relation with the PAEP climate. A state-based hidden Markov model was used to describe 46 December–May seasons (8372 daily rainfall sequences) at 68 stations. The HMM used here is fully presented and described in Robertson et al. (2004, 2006) and Greene et al. (2008). The HMM structure and assumptions are presented in the appendix. Briefly, for each location, conditional on state, the rainfall emitted by the model on a given day is drawn from a three-component mixture model (a delta function at zero amounts to model dry days and a two-component mixed-exponential distribution represents rainfall intensity). A preliminary examination of December–May daily rainfall distributions over the network showed that a two-component mixed-exponential model [Eq. (1)] is a valid assumption for representing rainfall amounts on wet as well as dry stations:

$$p(\mathbf{R}_t^m = r \mid S_t = i) = \begin{cases} p_{im0} & r = 0 \\ \sum_{c=1}^{C} p_{imc} \lambda_{imc} e^{-\lambda_{imc} r} & r > 0 \end{cases}, \quad (1)$$

where $\mathbf{R}_t$ is a multivariate vector of daily rainfall r; S_t is the hidden rainfall state for day t; λ are the parameters of exponential distributions; t is time in days; and indices i, m, and c refer to state, station, and mixture component, respectively. The p_{imc} are weights. In the summation, C refers to the number of exponential components. The prescription of number of states is an important step for the diagnosis goal. A small number of states is needed to allow physical interpretation, while a large number might add skill in generating synthetic series. In the HMM and NHMM used in this study, parameter estimation was performed by maximum likelihood, using the iterative expectation maximization (EM) algorithm (Dempster et al. 1977; Ghahramani 2001). The algorithm was initialized 10 times from random starting points, the run utilized being that with the highest log-likelihood. A numerical test using a larger number of random starting points showed that 10 initializations make a good compromise between computation time and estimation of the global maximum in the log-likelihood. The Bayesian information criterion (BIC; Schwarz 1978) was used to guide the choice of the number of states k and to assess the performance of different mixture models. The number of states was determined by fitting HMMs with 2–10 states under leave-3-years-out cross validation. The BIC (Fig. 4) showed that there is no overfitting when as many as 10 states are prescribed and that the two-component mixed-exponential model outperforms a single-exponential and a gamma model. A four-state model with two mixed-exponential distributions was thus chosen to represent the December–May rainfall. This was subjective, guided by the number of physically interpretable states. Models with a larger number of states showed state subsampling.

A final step for the weather state diagnosis involved identification of each state and its mapping onto large-scale circulation composites, as it provides the basis of the synoptic controls of the December–May rainfall and the physical ground for the downscaling using GCM information. The mapping of each state in terms of atmospheric composites involves 1) the identification of the days falling into each state, which is accomplished by means of the Viterbi algorithm (Forney 1973), a dynamic programming algorithm that returns the most likely sequence of states for the transition matrix of the four-state HMM, and 2) the collection of diagnosed days as representing each of the states in order to create atmospheric

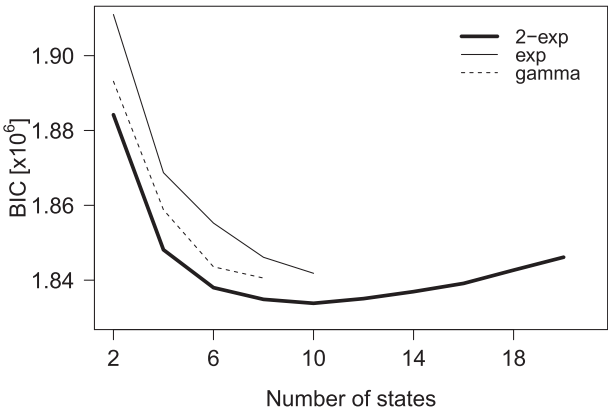

FIG. 4. BIC for fitted models with different numbers of hidden states: two-component mixed-exponential (thick), single-exponential (thin), and gamma (dotted) distributions for rainfall on wet days.

situations associated with each state. Composites were generated using NCEP–NCAR reanalyses (Kalnay et al. 1996) fields of specific humidity (qa) and horizontal winds at 850 hPa representing the lower circulation.

b. *Seasonal GCM information: Model and predictors selection*

Previous studies (Recalde-Coronel et al. 2014) have addressed the December–April seasonal rainfall predictability based on canonical correlation analysis (CCA) between observed SSTs, GCM predictions, and station-gridded rainfall over the entire Ecuadorian territory. However, their study looked up the entire Ecuadorian rainfall, and did not make a distinction of the climatic regions as described in, for example, Bendix and Lauer (1992). We revisited the analysis of Recalde-Coronel et al. (2014) and conducted a set of CCA experiments to 1) address the role of observed and predicted SSTs and GCM predictions on the predictability of the December–May rainfall over a network of 68 stations in the PAEP and 2) build up the best set of predictors to influence the transition matrix of the NHMM. CCA is a multivariate statistical method (Wilks 2006) widely applied in seasonal climate forecasting and as an analysis tool to investigate covariance and isolate linear relationships between datasets. The method calculates linear combinations of a set of predictors that maximizes relationships, in a least squares error sense, to similarly calculated linear combinations of a set of predictands. The CCA regularizes the high-dimensional regression problem between a spatial field of predictors and predictands by reducing the spatial dimensionality via principal component analysis (PCA) to minimize problems of overfitting and multicollinearity (Tippett et al. 2003). Thus, both predictors and predictands were

separately prefiltered using PCA prior to the CCA. In all CCA experiments in this study, a 5-yr cross-validation window was used to determine the truncation points of the CCA and the principal component (PC) series. That is, 5-yr running consecutive cases are held out, with the middle year predicted (and later verified) as a simulated independent case outside of the training sample (Barnston and van den Dool 1993).

1) GCM SELECTION

CFSv2 and ECHAM4.5 and observed SSTs were evaluated on their skill to hindcast the December–May seasonal rainfall amount using CCA. CCA regression models were fitted between seasonal (December–May) total rainfall over the station network and 1) December–May SST observations; 2) December–May CFSv2 SST predictions; and 3) ECHAM4.5hi (simulations), 4) ECHAM4.5ca (predictions), and 5) CFSv2 (predictions) for December–May ensemble-mean rainfall. The CCA regression models were trained and tested over the 1982–2010 period. The 28-yr period was taken as the common range with information among all GCMs. The spatial domain (15°N–15°S, 64°–100°W) was chosen as to allow correction of the GCM's spatial bias (Recalde-Coronel et al. 2014). From a physical point of view, this domain covers the Niño-1.2 region, the southernmost flank of the ITCZ, and the eastward expansion of the South American monsoon (SAM) system. Pearson correlation, bias, and root-mean-square error (RMSE) were computed to assess the quality of the hindcast December–May seasonal precipitation amount.

2) PREDICTOR SELECTION

CCAs were conducted between the GCM seasonal ensemble-mean rainfall (identified in the previous step) and the December–May rainfall total amount over 1) the entire network and 2) three subsets grouped according to elevation ranges [<510 (35 stations), 511–1900 (14 stations), and >1901 m MSL (19 stations)]. These subsets were needed to capture modes of variability that can be associated with a dominant rainfall regime in a given region (Pineda et al. 2013) and to investigate the sensitivity of the CCA to the choice of the sampling domain. Namely, four CCA models were fitted with prescribed model settings (prefiltered GCM PCs/station-network rainfall PCs) to maximize the discriminatory power between the GCM explanatory fields and the rainfall response variable. In the regional analysis, three GCM PCs were regressed onto three seasonal rainfall PCs, whereas, in the elevation-dependent analysis, three GCM PCs were regressed onto one seasonal rainfall PC. The former was used to investigate the modes of variability relevant for the entire region; the latter was used to isolate the driving mode for each elevation range. The identified CCA and PC modes were ranked and compared with the weather states identified via the HMM, leading to a more physically sensitive predictor selection.

c. *Downscaling seasonal GCM information*

1) CCA MODEL

We use the best GCM identified in section 3b(1) and apply CCA directly to downscale the seasonal rainfall statistics of interest. As predictor fields, the retrospective December–May ensemble-mean rainfall was regressed onto the December–May seasonal amount, wet-day frequency, and mean daily intensity. The CCA models were trained over the 1974–2010 period and used to hindcast 36 December–May seasonal aggregated rainfall statistics. We restrict the model fitting to 36 seasons because data quality was better for that period (fewer missing gaps). In this way, the CCA-based hindcast provides a benchmark against which the GCM–NHMM simulations are compared at a seasonal aggregated level.

2) NHMM

Weather states are inferred from patterns of observed daily precipitation and modeled as first-order Markov dependent in time, while a large-scale circulation index is utilized as a predictor in a multinomial logistic regression, the dependent variables being the probabilities in the Markovian transition matrix (Greene et al. 2011). Spatial dependence is implicitly captured by the existence of multiple states while the temporal dependence is captured via the Markov property of the state transition process. The four-state HMM was expanded to its nonhomogeneous version by allowing the transition matrix to introduce the best predictors identified in section 3b(2). These covariates were identified from the GCM outputs as cross-validated CCA modes and related to the state–state transition probabilities according to the polytomous logistic regression (Robertson et al. 2004):

$$p(S_t = j \mid S_{t-1} = i, \mathbf{X} = x) = \frac{\exp(\sigma_{ij} + \rho_j x)}{\sum_{k=1}^{k} \exp(\sigma_{ik} + \rho_k x)}, \tag{2}$$

where p is the transition probability and $i \rightarrow j$ is the transition from time $t - 1$ to t, given the value x of predictor $\mathbf{X}$ at time t (days). The parameters σ_{ij} and ρ_j are real-valued parameters and D-dimensional real-valued parameter vectors, respectively, which need calibration. The number of states k equals 4.

The four-state NHMM was fit to 36 December–May seasons (6336 daily rainfall sequences) within 1974–2010 at 68 stations together with the leading CCA mode (best

predictor). The CCA mode was linearly interpolated to daily resolution prior being used as univariate input and influences the transition matrix of the NHMM. Parameter estimation was performed using the EM algorithm as described in section 3a. The NHMM was trained under leave-one-year-out cross validation, so that for each fold of the cross validation the CCA mode was derived anew for each left-out set of years. To make downscaled simulations, the trained NHMM was used in conjunction with the daily interpolated CCA-mode input to generate 100 daily simulations of rainfall. This yielded an ensemble hindcast of 100 daily rainfall sequences for each December–May season. The daily rainfall ensemble emitted by NHMM was drawn from a three-component mixture model (section 3a). The model comprises the exponential parameters and mixing weights [Eq. (1)], and the matrix of probabilities governing day-to-day transition among states. The CCA-mode covariate will then influence the state characteristics (probabilities and intensities) for each of the stations on a daily basis. Notoriously, the present GCM–NHMM approach is designed to map the value of a skillful input predictor, summarized from the GCM's ensemble mean via CCA. Hence, its ability to produce statistically reliable conditional distributions will strongly rely on the ability to extract such input information from the GCM forecast as well as on the emission model's skill to represent probabilities and intensities across the network. In addition, the GCM-CCA calibration step constrains the present modeling approach to produce a probabilistic ensemble that does not incorporate the distribution across all GCM ensemble members.

The statistics of interest (seasonal amount, probability of occurrence, and mean daily intensity) were evaluated at regional scale to compare both downscaling approaches. Daily rainfall simulations were converted to hydrologically relevant characteristics and aggregated at catchment level. The hydrological verification statistics were chosen considering the fact that the downscaled daily rainfall eventually forms an input for hydrological outlooks. Thus, the focus was on metrics relevant for seasonal water availability (seasonal amount) and rainfall–runoff generation process [maximum number of consecutive wet days ($>1.0\,\mathrm{mm\,day^{-1}}$)]. Also, extreme rainfall indices such as high daily rainfall (99th percentile of daily rainfall that is exceeded on average 3–4 times a season) and high 3-day rainfall total (99th percentile 3-day accumulated rainfall per season; Fu et al. 2013) were considered. These indices may indicate high runoff generation in catchments with a short response time as is the case over mountainous regions.

4. Results and discussion

a. *HMM weather states*

1) Description and transitions

Figure 5 shows wet-day probabilities and mean intensities for the four-state HMM. The HMM decomposes the December–May rainfall into one well-differentiated pair of wet states, one dry state, and one transitional state. State 1, which we ranked as the wettest state, exhibits high probabilities and intensities everywhere. Conversely, state 2 might be regarded as the driest. The latter state shows regionwide dry conditions except for top of the western Andean foothills (>2000 m MSL). State 4 shows also wet conditions, which are greater over the northern catchments, while state 3 shows transitional dry and wet conditions that follow the relief of the Andean and coastal cordilleras.

The stationary transition matrix of the four-state model is presented in Table 1. This matrix represents a mechanistic description of the temporal dependency of the observations in a probabilistic form. The entries in the matrix show the day-to-day conditional probabilities of the state transitions. Note that the transition from state 1 to 2 (from the wettest to the driest) and vice versa are unlikely to occur (0.003) so that state 3 interfaces between wet and dry conditions. Namely, the dry–wet state 3 likely evolves to a drier state 2 (0.174). This suggests that HMM captures the underlying rainfall dynamics well, and from a process-oriented point of view, it supports the concept of a drier onset (December–January) and a wetter and sudden retreat (April–May) of the rainy season [see also section 4a(3) and Fig. 7, described in greater detail below].

2) Synoptic conditions

Figure 6 shows anomalies of composites of NCEP–NCAR reanalyses of specific humidity and horizontal winds fields at 850 hPa for each diagnosed state together with the state rainfall probabilities. Both atmospheric composites and state rainfall probabilities are expressed as anomalies with respect to the December–May climatology. We describe the December–May climatological ITCZ migration prior to discussing the states in terms of atmospheric composites. During December–February, the ITCZ reaches its southernmost position near the equator in the eastern Pacific influenced by vigorous northeastern trade winds over the Central American isthmus and the weakening of the southern trade winds. In contrast, during June–August the southeastern Pacific anticyclone is at its northernmost position, the South Pacific trade winds become stronger, and the ITCZ stays north of the equator. State 1 (1523 days), the wettest

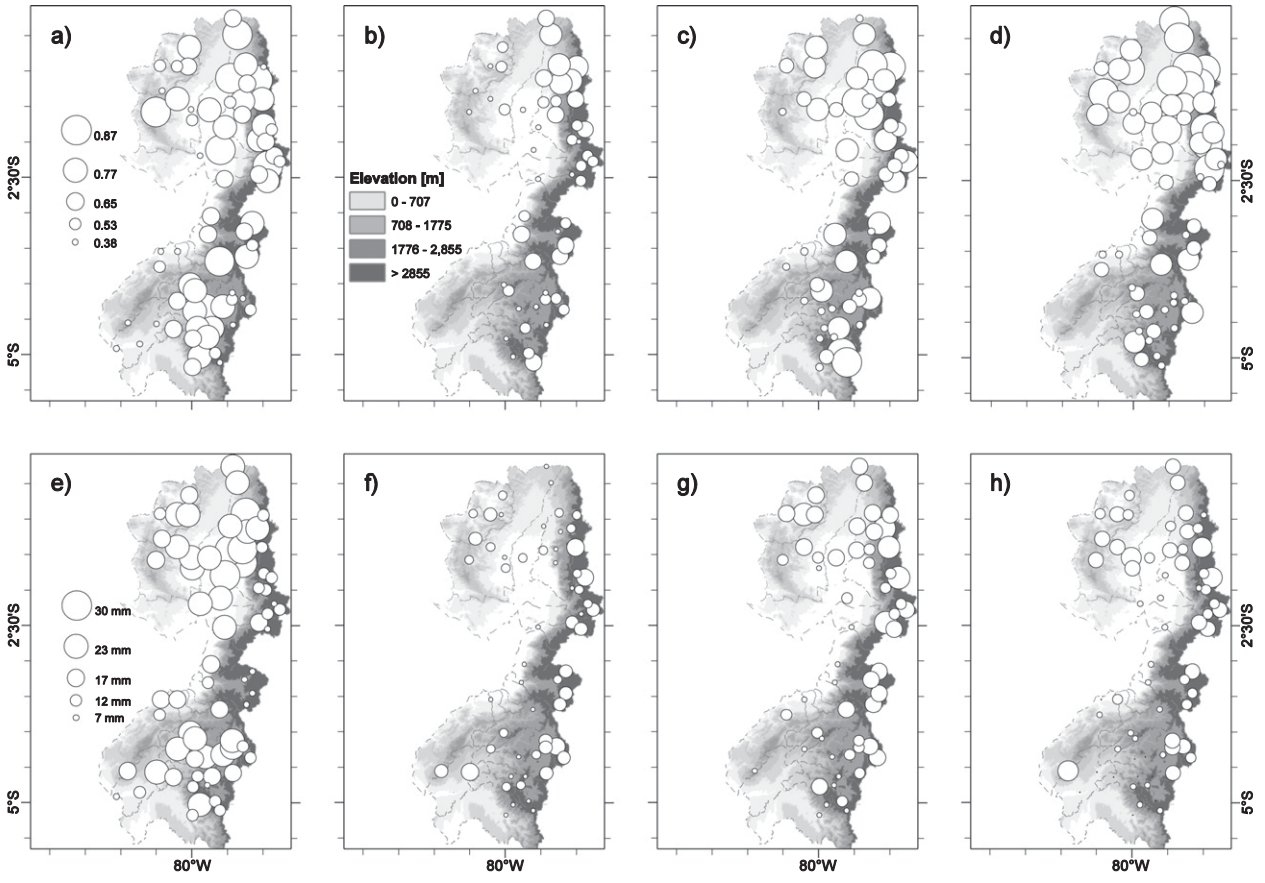

FIG. 5. (a)–(d) Occurrence probabilities and (e)–(h) mean wet-day (≥0.1 mm) intensities (mm) for the four-state model. States 1–4 are shown from left to right. The legend in (a) applies to (b)–(d) and the legend in (e) applies to (f)–(h).

state, appears as a surplus of atmospheric moisture offshore of the PAEP, south of about 3°N, and bounded by the Andes relief (Fig. 6a). This situation is accompanied by weak landward winds that seem deflected southward by the Andes. In this setting, the PAEP seems exposed to warm air masses penetrating into the innermost valleys and driving the occurrence of wet days everywhere with maxima centered within February–April (Fig. 7). Conversely, state 2 (2833 days), the driest one, shows the coolest maxima of atmospheric moisture together with an adynamic lower-level wind zone offshore of the southern coast of the PAEP (~5°S). This driest maxima configuration imprints an opposite signal to that of the wettest state with negative rainfall probability anomalies over the dry border area of Ecuador and Peru. State 3 (1583 days) shows positive rainfall probabilities for the highest Andes elevations and negative over the bottom valleys. The accompanying synoptic situation is less clear, showing neutral atmospheric moisture conditions with well-developed easterlies, still impinging wet conditions on the higher stations (Fig. 6c). The counterpart atmospheric situation for the wet state 4 (2433 days) (north–south gradients with larger probabilities and intensities north of 2.5°S) exhibits two maxima of atmospheric moisture (boxes in Fig. 6d). We hypothesize that this situation is more dynamically driven by the southernmost displacement of the ITCZ and to a lesser extent by the eastward expansion of the SAM. We will later demonstrate that the former is more likely and that this situation is key in driving season-lasting wet conditions in the PAEP.

3) SEASONAL AND INTERANNUAL VARIABILITY

Figure 7 reveals a systematic progression in the state occurrences over December–May. During December,

TABLE 1. Transition matrix for the four-state HMM. For example, the probability of a transition from state 2 to state 4 is 0.093.

		"To" state			
		1	2	3	4
"From" state	1	0.685	0.003	0.187	0.126
	2	0.003	0.799	0.105	0.093
	3	0.112	0.174	0.564	0.150
	4	0.170	0.090	0.121	0.619

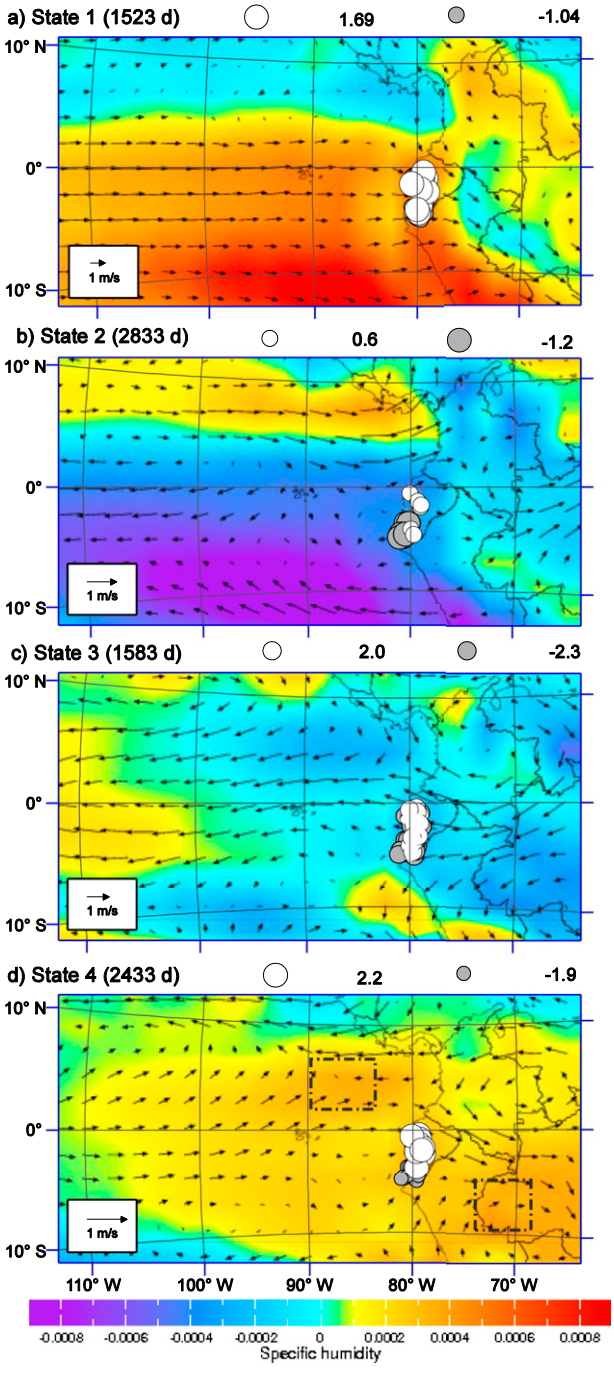

FIG. 6. HMM state anomaly composites of horizontal winds (vectors) and specific humidity at 850 hPa (colors) with respect to December–May climatology for 1964–2010 together with rainfall anomaly probabilities at each station (circles). (a)–(d) States 1–4, respectively.

the drier state 2 dominates while in the middle of the rainy season (February–April) states 1 and 4 show major importance. State 3, which we argue to play a transitional role, appears as the bridge between dry–wet conditions in

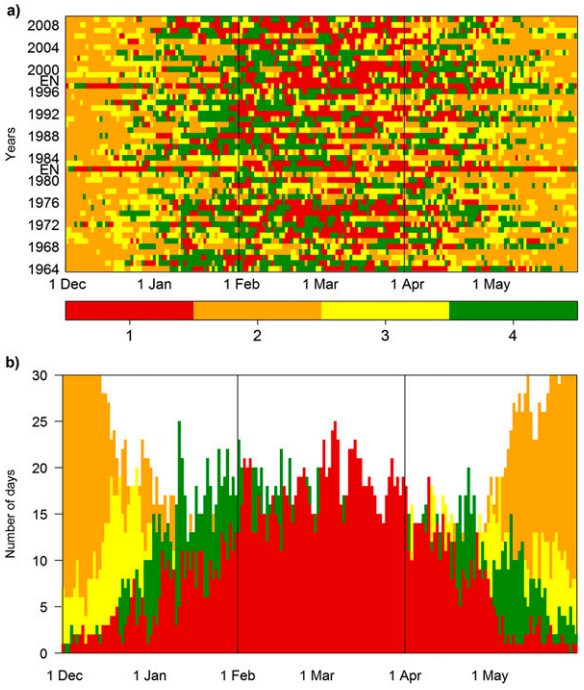

FIG. 7. (a) Viterbi sequence of most likely states 1964–2010. (b) Corresponding daily climatology, clustering of days in state over the 46-yr period. Colors indicate states 1–4.

December–January and conversely wet–dry conditions in May. Its importance diminishes in the core of the mature phase (February–April). Also, Fig. 7b reveals that the wet state 4 is important in generating wet conditions in the onset (January–February) and the retreat phase (April–May) of the rainy season.

Figure 7a also unveils important features of intraseasonal and interannual variability. First, it can be noticed that within the early development of the mature phase (January–March) state 4 precedes state 1 during almost the entire 46-yr period. In the next phase (March–April), state 1 emerges as predominant, concomitant with the occurrence of maximum SSTs in the eastern Pacific, which tend to peak around March–May (Vuille et al. 2000; Pineda et al. 2013). The exceptions are El Niño years (1983–97) for which the persistence of state 1 is season-lasting amplified. To study the interannual variability of state occurrence (IVO), this is plotted in terms of the number of days assigned to state 1, normalized by its standard deviation, together with December–May Niño-1.2 index (Fig. 8a; Pearson correlation is 0.72). This suggests a synchronized response of state 1 to the Niño-1.2 index. We conclude that state 1 is thermally induced by SSTs that fuel atmospheric moisture building up the primary source for the December–May rainfall in the PAEP.

Figure 8b shows the partial autocorrelation function (ACF) of the IVO for state 4. The ACF shows an

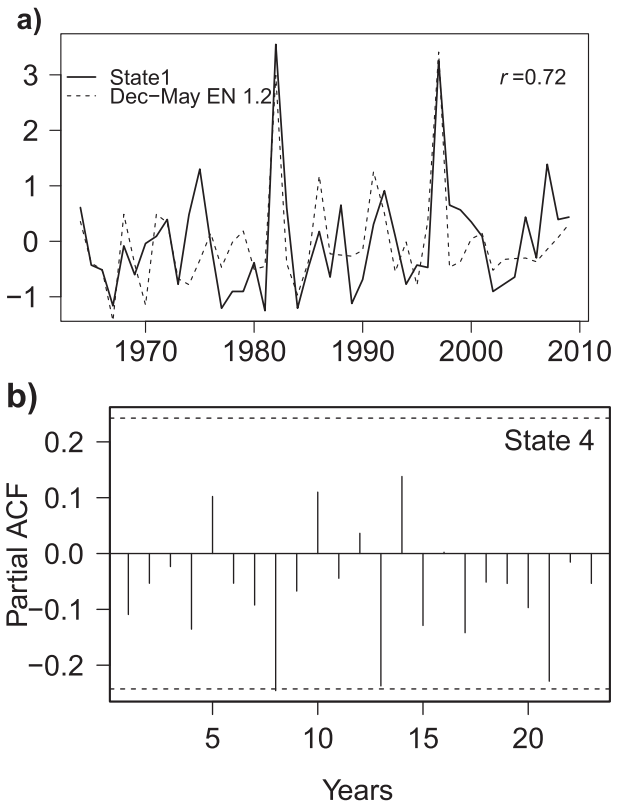

FIG. 8. (a) IVO for state 1 together with December–May Niño-1.2. (b) Partial ACF of IVO for state 4 with 90% confidence bands.

alternating sequence of positive and negative values not decaying at zero. Negative values are larger at 4, 8, 13, 17, and 21 lag (8 lag is statistically significant at the 90% level). However, this does not support evidence that state 4, which is associated with wet conditions (larger number of wet days than state 1), may originate from a cyclical process being modulated at interannual scales. The IVO of state 2 shows an opposite sign to that of state 1. The Pearson correlation between the normalized IVO of state 2 and the Niño-3.4 index is −0.14, which does not show a connection with La Niña conditions. The IVO of state 3 shows the occurrence of two minima in the years 1982 and 1997, which precede the wettest years in the records.

b. GCM information

1) SEASONAL MODEL SELECTION

Figure 9 shows Taylor diagrams (Taylor 2001) of the cross-validated seasonal hindcast 1982–2010 period obtained by regressing contemporaneous (December–May) SSTs and the GCM seasonal-average rainfall predictions and simulations onto the observed station seasonal rainfall amounts. Note that hindcasts that make use of observed SSTs are not true predictions. These figures summarize both aspects of model performance, the correlation coefficients and normalized standard deviation. The correlation between the prediction and observed reference variable is given by the azimuthal position. The radial distance from the origin is proportional to the normalized standard deviation. The coordinate position marked by a dot on the *x* axis represents the perfect match between prediction and observation. The hindcast made using coincident SSTs shows the highest correlations but underestimates the dispersion from the reference deviations. CFSv2 shows low performance in R2, R3, and R4; even lower performance is found when predicted SSTs are used as the predictor. The lack of skill of CFSv2 to hindcast SSTs anomalies in the central and equatorial Pacific, that is, underestimation of the 1982/83 and 1997/98 anomalies in the Niño-1.2 region (Takahashi et al. 2014), would explain that low performance. What is important in our set of experiments is the sensitivity of the ECHAM4.5 when driven by observed (ECHAM4.5hi) and predicted SST (ECHAM4.5ca). We find that when ECHAM4.5 is forced (corrected) with observed SSTs, the model improves predictive performance. This is because the corrected ECHAM4.5 reproduces as dominant mode an El Niño–like rainfall signal leading to a better representation of the higher seasonal amounts. In fact, the leading ECHAM4.5hi PC score, after truncation in the CCA, shows a correlation of 0.72 with the Niño-1.2 index. In contrast, the leading ECHAM4.5ca PC score in the CCA regression model does not depict an El Niño–like signal and its spatial pattern shows a dipole-like structure with high loadings north and south of the equator. The bias reduction seen in ECHAM4.5hi (R1, R2, and R3) underscores the importance of the atmospheric GCM's component in simulating the whole range of regionwide seasonal rainfall totals. Figure 10 shows Pearson correlation skill maps for all hindcast experiments. The SST-based hindcast correlates with topography, where the highest correlations take place on the bottom valleys, and they sharply decrease over the highlands (>1700 m MSL; Fig. 10a). The ECHAM4.5hi and ECHAM4.5ca hindcasts (Figs. 10b,c) show, in turn, less marked spatial trends with high correlations over the northern catchments. CFSv2 (Fig. 10d) shows the lowest performance regionwide. Therefore, we focused on both the ECHAM4.5 simulations and retrospective forecasts in order to build up a set of predictors to downscale seasonal retrospective information to station daily characteristics.

2) GCM CALIBRATION: PREDICTORS SELECTION

We have provided evidence that an important component of the December–May rainfall is dictated by the

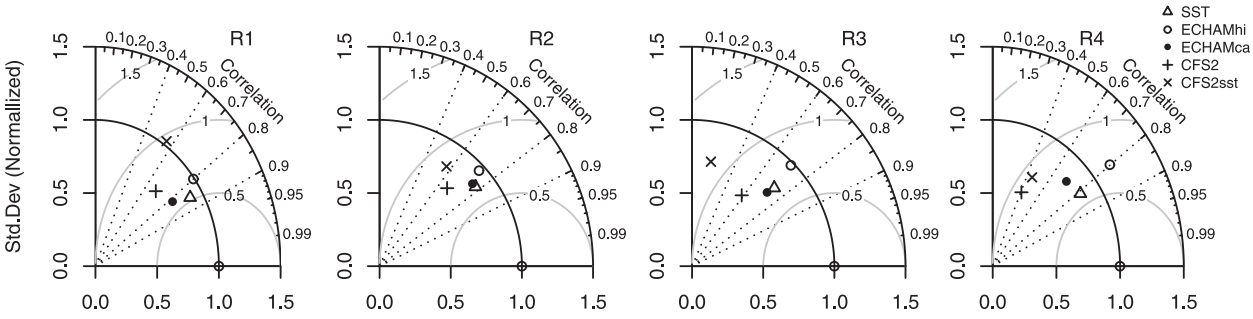

FIG. 9. December–May predictive performance of cross-validated hindcast over four hydroclimate zones in the PAEP using CCA for concurrent SST, CFSv2-predicted SST, one-season-lagged ECHAM4.5hi, ECHAM4.5ca, and CFSv2 for 1982–2010.

SST conditions over the eastern Pacific, but there is also an important GCM component that might be instrumental for prediction over the Andean foothills. The question then arises of which GCM (ECHAM4.5) information better captures the PAEP rainfall signal. Table 2 summarizes the CCA between SST observations and retrospective ECHAM4.5hi and ECHAM4.5ca (simulation and predictions) for the December–May mean atmospheric fields regressed onto the December–May station rainfall for the entire region and each altitudinal range. The evaluation metrics include the canonical correlation coefficient (CC), which shows the strength of the linear correlation between the time series of the coupled patterns, and the spatial average Pearson correlation ρ_{average}. The number of canonical coupled modes (regional analysis) and the number of retained GCM modes is also presented. The best predictor is found, being the leading canonical mode of the ECHAM4.5hi (ECHAM4.5hi CC) because it shows the highest ρ_{average} in the regional as well as the elevation-based analysis, but <510 m MSL where observed SSTs are a better predictor. Among the predictor fields from ECHAM4.5ca, the specific humidity at 850 hPa (qa850) followed by the precipitation field (prec) emerge at the forefront. The temperature and horizontal wind fields of the lower troposphere (temp850 and uv850) showed poorer predictive skill. An exhaustive description on the loss of predictive skill when using ECHAM4.5ca outputs is out of the scope of this study. Therefore, we only highlight the major differences as revealed by inspecting the temporal and spatial components in the CCA regression models.

In general, the qa850 predictor field showed better performance than the prec predictor field (Table 2). This appears to be related with the GCM limitation inherited from the imperfections in predicting the SSTs to force ECHAM4.5ca. Evidence of this is found in the two GCM modes that are retained to build the leading canonical variate for the qa850-based regression model. While the first one shows a weak El Niño–like flavor in both the temporal and spatial patterns, the PAEP rainfall signal is better spotted in the second mode. This signal has a spatial structure showing high loadings offshore of the PAEP. Similar patterns are not detected in the canonical variate derived from the prec-based

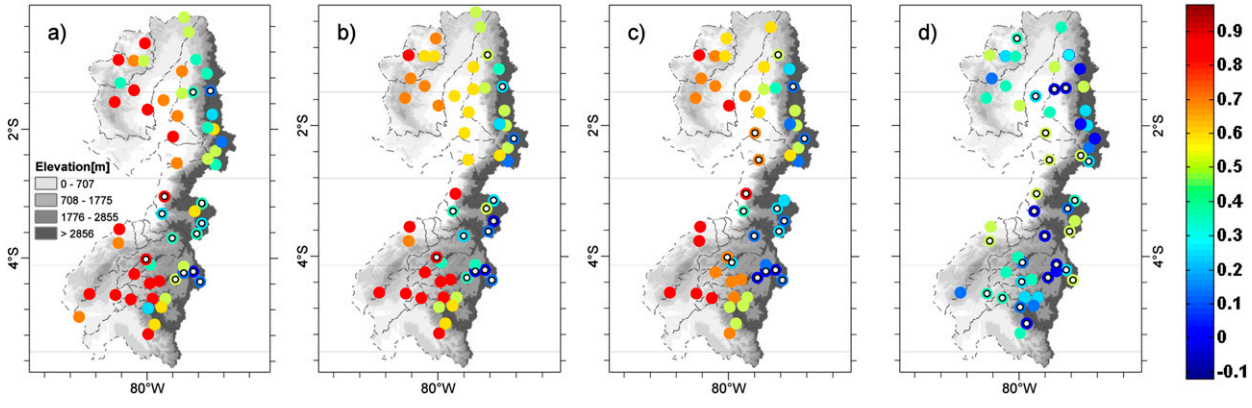

FIG. 10. Pearson correlation between seasonal accumulated precipitation amounts and CCA hindcasts for (a) concurrent SSTs, (b) ECHAM4.5hi, (c) ECHAM4.5ca, and (d) CFSv2 retrospective predictions for 1982–2010. White dots indicate values not significant at the 95% level.

TABLE 2. CCA between December–May station rainfall and SST observations and ECHAM4.5hi and ECHAM4.5ca for different atmospheric fields: prec, qa, temp, and uv at the lower troposphere (850 hPa). The evaluation metrics are the CC and ρ_{average}. The cumulative GCM explained variance retained in the CCA models [$\Sigma(\text{Variance}_{\text{GCM}})$; %] is also presented.

		ECHAM4.5hi	ECHAM4.5ca			
	SST	prec	prec	qa850	temp850	uv850
PAEP						
CC (ρ_{average})	0.90[a] (0.39)	0.77[a] (0.48)	0.45[a] (0.03)	0.49[a] (0.15)	0.41[a] (−0.20)	0.38[a] (−0.18)
No. of CC modes	3	2	2	2	1	2
No. of modes in GCM (obs)	3 (3)	2 (2)	3 (3)	2 (2)	3 (2)	3 (2)
$\Sigma(\text{Variance}_{\text{GCM}})$ (%)	96.22	61.29	56.32	84.00	99.31	81.45
>1901 m						
CC (ρ_{average})	0.49 (0.08)	0.54 (0.24)	0.45 (0.05)	0.48 (0.17)	0.36 (−0.01)	0.39 (−0.07)
No. of modes in GCM (obs)	3 (1)	2 (1)	3 (1)	2 (1)	3 (1)	3 (1)
$\Sigma(\text{Variance}_{\text{GCM}})$ (%)	96.68	60.47	71.88	84.51	99.26	81.23
511–1900 m						
CC (ρ_{average})	0.72 (0.26)	0.72 (0.42)	0.34 (−0.08)	0.36 (0.01)	0.24 (−0.28)	0.36 (−0.24)
No. of modes in GCM (obs)	2 (1)	3 (1)	1 (1)	2 (1)	3 (1)	3 (1)
$\Sigma(\text{Variance}_{\text{GCM}})$ (%)	92.44	75.57	32.26	83.58	99.31	81.5
0–510 m						
CC (ρ_{average})	0.86 (0.63)	0.75 (0.62)	0.39 (0.07)	0.46 (0.29)	0.11 (−0.25)	0.26 (−0.11)
No. of modes in GCM (obs)	2 (1)	2 (1)	3 (1)	3 (1)	1 (1)	1 (1)
$\Sigma(\text{Variance}_{\text{GCM}})$ (%)	93.09	60.59	56.21	92.83	97.7	52.87

[a] Leading CC mode.

regression model. In the latter model, the first retained GCM mode resembles a dipole-like pattern as described in section 4b(1) with the PAEP rainfall signal again placed in the second mode. Thus, it might be thought that a weak or imperfect lower boundary forcing constrains the ECHAM4.5ca skill for emulating thermally driven rainfall, which we argue to be a major component of the PAEP rainfall.

Figure 11 shows the calibrated leading cross-validated ECHAM4.5hi canonical series (ECHAM4.5hi CC) (first row, second column of Table 2). The station-averaged rainfall amount and its standard error are also shown. Note the high correlation of 0.89. Also, the normalized ECHAM4.5hi and ECHAM4.5ca (simulation and prediction) seasonal-mean and pixel-wise spatial averages over the PAEP (0°–6°S, 78.5°–82°W) are plotted; their linear correlations with observations are 0.87 and 0.43, respectively. Differences are high between the simulation and prediction outputs of the GCM, which illustrates the loss of skill in the GCM when the lower boundary forcing switches between SST observations and predictions. The performance of the ECHAM4.5hi spatial average over the PAEP is high, particularly in the wettest years (1983, 1987, 1992, and 1998), but it decreases for the non–El Niño and normal years. The improvement achieved by calibrating ECHAM4.5hi then comes through a better representation of the low values of the station-averaged observations. This is because the leading ECHAM4.5hi CC retains two GCM modes in the regional as well as in the elevation-dependent analysis (Table 2). Below, we show that such modes summarize much of the physically relevant information and they provide the canonical variate with the signal-to-noise ratio observed in the PAEP rainfall.

Figure 12a shows the spatial structure of the first retained ECHAM4.5hi PC, where two regions of maximal rainfall anomalies appear over the PAEP and the Galapagos Islands. This configuration might be regarded as the ECHAM4.5 model response to the SSTs' perfect forcing. That is, when SST observations are used as the lower boundary, the ECHAM4.5hi (simulation)

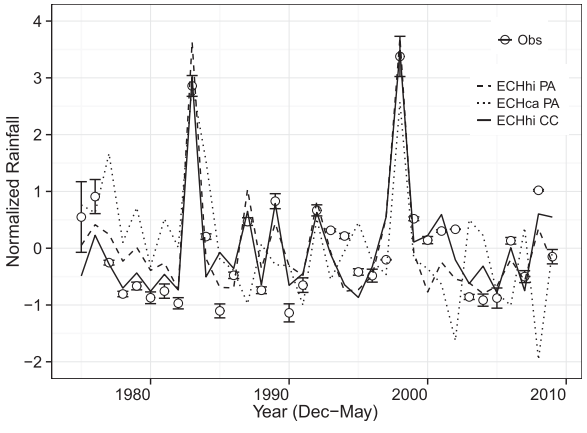

FIG. 11. Interannual variability of candidate GCM predictor variable together with the observed seasonal accumulated total, averaged over the PAEP, with the error bars representing observation standard errors. All curves have been normalized by its interannual std dev.

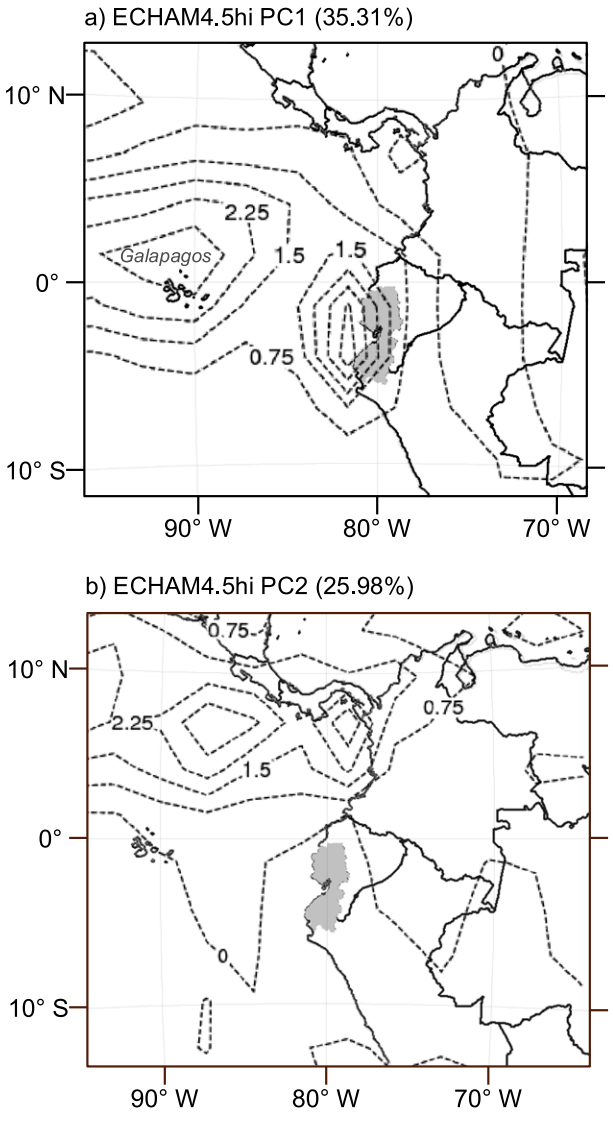

FIG. 12. Leading PCs of precipitation for the ECHAM4.5hi (15°N–15°S, 64°–100°W; dashed contour lines). The explained variance is given in parentheses. The amplitudes of the loadings correspond to one std dev yearly anomaly. PAEP is shaded in gray.

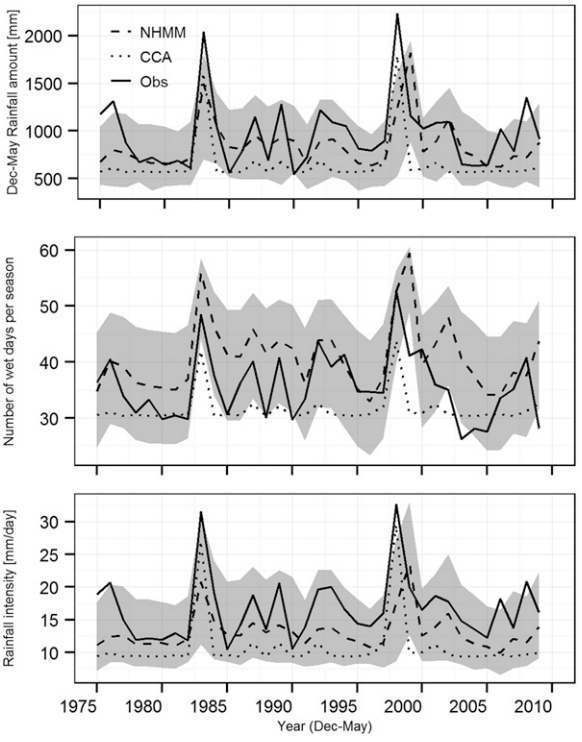

FIG. 13. Interannual variability of NHMM-simulated seasonally averaged rainfall (top) amount, (middle) occurrence frequency, and (bottom) intensity (average amount on wet days). Plotted is the median of 100 NHMM simulations averaged over the PAEP (solid) vs the CCA-based hindcast (dotted) and the observed (dashed). The interquartile range is shaded in gray.

December–May rainfall signal resembles the spatial patterns of the ITCZ during El Niño years, depicting two maxima over the Niño-1.2 and the eastern edge of the Niño-3 regions. The structure of the second ECHAM4.5hi PC (Fig. 12b) shows a maximum (5°–9°N) that we refer to as the northern position of the ITCZ during non–El Niño years. Notice the spatial consistency between the geospatial patterns detected by calibrating ECHAM4.5hi via CCA (36 seasons) and the spatial configuration of the diagnosed states 1 and 4 via the HMM (46 seasons; Figs. 6a,d), despite that the latter was mapped onto NCEP–NCAR reanalyses fields. This provides the climate drivers characterization robustness regarding the identity of the physical mechanisms controlling the December–May rainfall in the PAEP.

c. *CCA hindcast*

Figure 13 shows the CCA-based hindcast in terms of station-averaged December–May rainfall statistics of interest together with observed values. Pearson correlation coefficients between the hindcast and observations are high for the three statistics: seasonal amount ($\rho = 0.83$), number of wet days per season ($\rho = 0.71$), and mean daily intensity ($\rho = 0.82$). The CCA model largely removes the bias seen in ECHAM4.5hi, particularly for the frequency of wet days that shows overestimation during the hindcast period. However, the natural variability is not well represented. A well-known drawback of estimates produced in a least squares sense is that they underestimate the natural variability (Lettenmaier 1994). Figure 14 shows Pearson's correlations between the seasonal rainfall amount, number of wet days, and mean intensity (wet days) per season produced by the CCA model and the observations. The southern region (R4) followed by the ocean-exposed

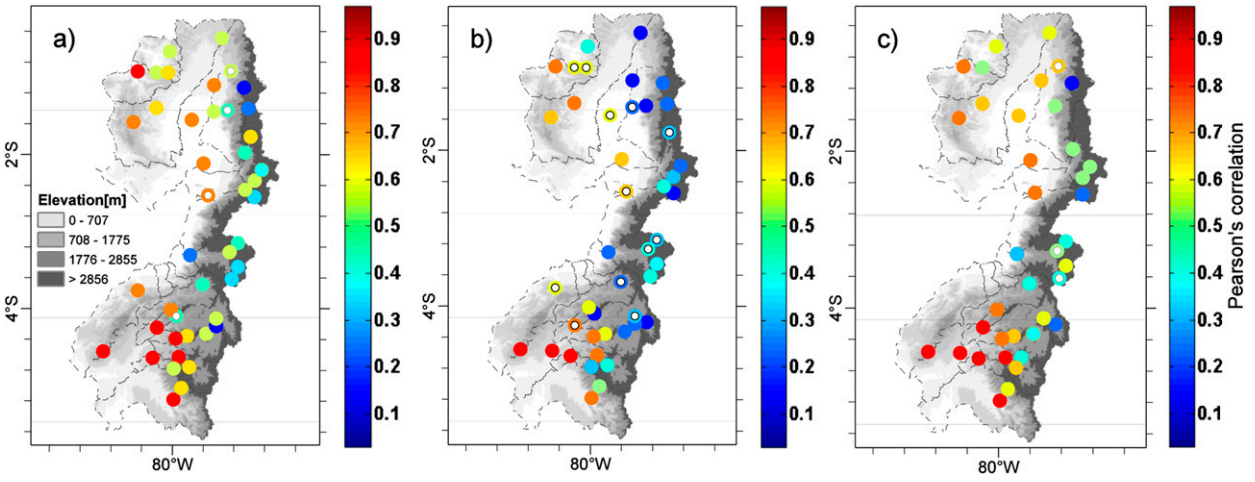

FIG. 14. Pearson's correlation between ECHAM4.5 historical simulations downscaled using the CCA model and observations for (a) seasonal rainfall amount, (b) number of wet days, and (c) mean rainfall intensity for 1974–2010. White dots indicate values not significant at the 95% level.

catchments in R1 show high correlations for the seasonal accumulated amount and mean intensity.

d. *NHMM simulations*

The NHMM, trained in cross-validated mode, as described in section 3c(2) using the calibrated canonical variate of the ECHAM4.5hi (simulations; ECHAM4.5hi CC), was used to generate 100 stochastic daily simulations of the December–May rainfall at 68 stations. Figure 13 shows the NHMM simulations in terms of the seasonal means averaged over the PAEP; the median and the interquartile range of the seasonal rainfall statistics of interest are plotted versus observations. Although the NHMM underestimates the highest seasonal total amounts observed during the wettest years (1983 and 1998), it reproduces the interannual variability of this seasonal accumulated and region-averaged quantity well ($\rho = 0.60$). The interannual variability of the number of wet days per season is less well simulated ($\rho = 0.50$); the NHMM overestimates this value during almost the entire hindcast period. The mean rainfall intensity of wet days shows the highest skillful hindcast ($\rho = 0.64$) and similar interannual variability than the seasonal aggregated quantity. Figure 15 shows Pearson's correlations and mean biases (normalized) between the seasonal rainfall statistics of interest derived from the NHMM ensemble mean of daily rainfall simulations and observations. The spatial pattern of correlations follows that obtained from the CCA-based hindcast but lower values regionwide. The largest positive biases for the number of wet days are seen over the northern edges in R1 and R2 (Fig. 15e). We hypothesize that the latter is related to the spatial correlation model used in the NHMM. The NHMM is parameterized to simulate the mean daily correlation structure across a network of stations. This is done on a weather state basis, via dependencies between neighboring stations, to account for the cross correlation associated with the distinct spatial rainfall patterns of each state. In such spatial parameterization, the complex spatial dependences of rainfall occurrences over the inner-Andean catchments are not accurately captured by the NHMM.

Figures 16a–d show Pearson's correlation between the hydrologically relevant characteristics and observations. The daily rainfall statistics were computed on a seasonal basis and then averaged at catchment level. The seasonal rainfall total (Fig. 16a) at the catchment scale preserves the skill observed at regional level. It is well reproduced in most of the hydrological units (about 50% of catchments show a correlation greater than 0.4). The highest correlations are encountered on coastal catchments south of 4°S: Tumbes (20), Piura (21), and Chipilco (19) and over the coastal catchments in R1: Chone (1), Portoviejo (2), and Lower Guayas (3). The extreme characteristics, the 99th percentile of the daily rainfall (Fig. 16b) and the 3-day rainfall total (Fig. 16c), are less well represented by the NHMM. Pearson's correlations, greater than 0.4, for both characteristics were found only over the southern region. This is a considerable loss of skill when reproducing extreme daily statistics as compared with the mean rainfall intensity value (Fig. 15c). Figure 16d shows the maximum number of consecutive wet days ($>1.0\,\text{mm day}^{-1}$). For this statistical metric, the NHMM shows the lowest performance in simulating observed values, likely related to the NHMM tendency to overestimate the number of wet days. Nevertheless, the NHMM hindcast also reduces the bias seen for this quantity as compared to the raw GCM data.

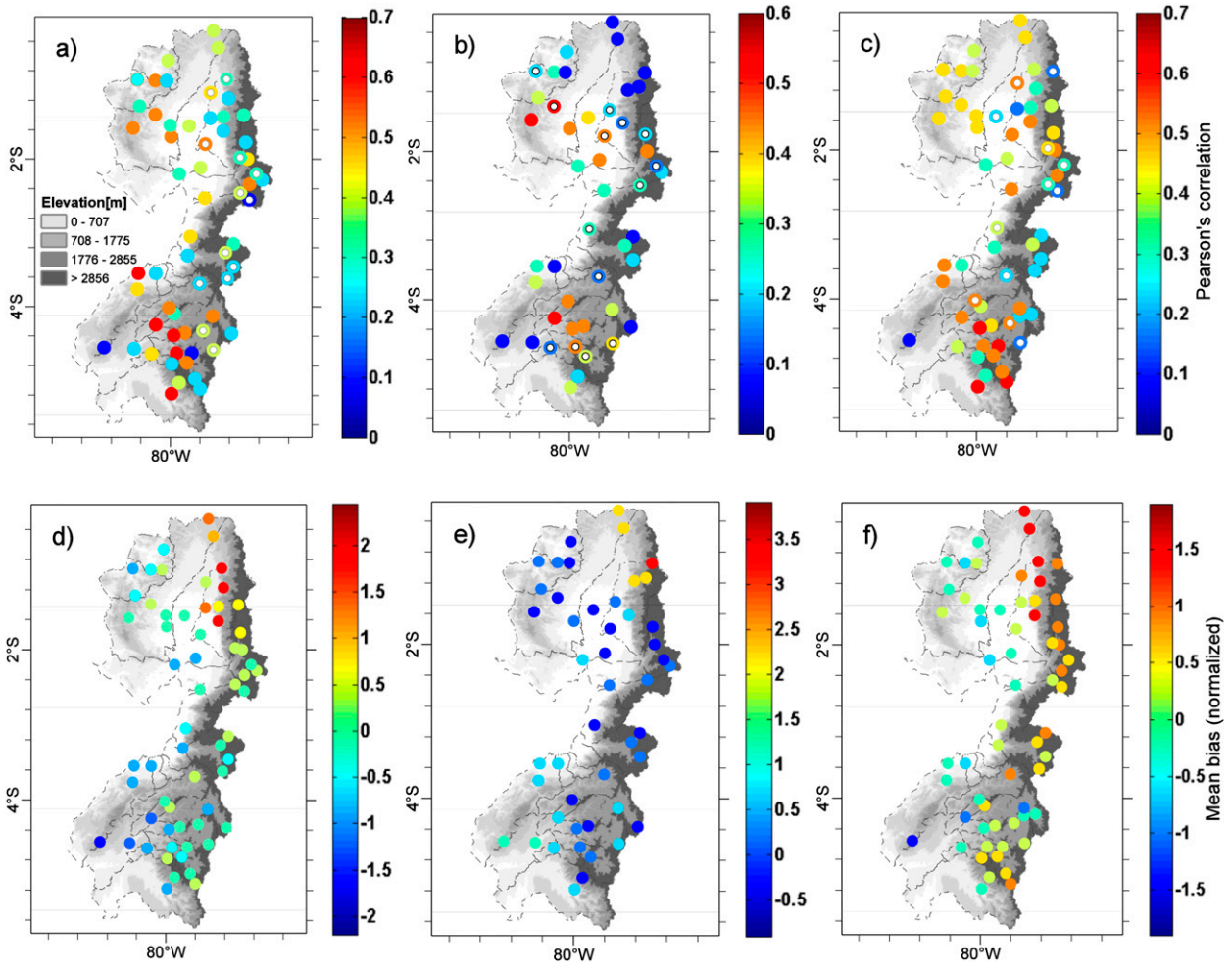

FIG. 15. (top) Pearson's correlation and (bottom) normalized mean bias between ECHAM4.5 historical simulations downscaled using NHMM and observations taking the ensemble mean over the 100 NHMM simulations for (a),(d) seasonal rainfall amount; (b),(e) number of wet days; and (c),(f) mean rainfall intensity for 1974–2010. White dots indicate values not significant at the 95% level.

5. Summary and conclusions

We have examined the seasonal predictability of December–May daily rainfall characteristics over a network of 68 stations in 21 catchments of the PAEP. In a first step, we used a hidden Markov model (HMM) to analyze daily rainfall occurrence and intensity to diagnose states related with the large-scale ocean–atmosphere forcing within 46 seasons (1964–2010). Then, we expanded to a nonhomogeneous HMM (NHMM) version and coupled it with GCM's retrospective simulations to assess the ability of a GCM–NHMM approach to derive regional and catchment hydrologically relevant information.

A four-state HMM was found effective in capturing key seasonal and interannual features of the rainy season in the PAEP. The diagnosed states fell into two wet states, one dry state, and one transitional state, which were found to play distinct roles in the onset, maturation, and retreat phase of the rainy season. The first wet state represents regionwide wet conditions and could be associated with a surplus of atmospheric moisture offshore of the PAEP, reaching the innermost valleys and driving wet occurrences everywhere. The identity of this wet state may be regarded as thermally induced, in which the climatological maximum of SSTs fuels warm air masses, building up the primary source of the PAEP rainfall. The second wet state was found to correspond with the dynamically noisy component of the PAEP rainfall signal. Evidence of this description rests on the state seasonal evolution (Fig. 7b), which shows that state 4 precedes 1 during almost the entire 46-yr period concomitant with the timing of the southern displacement of the ITCZ. Thus, on average, states 1 and 4 describe the wet properties of the seasonal cycle of the December–May rainfall. The dry state 2 shows

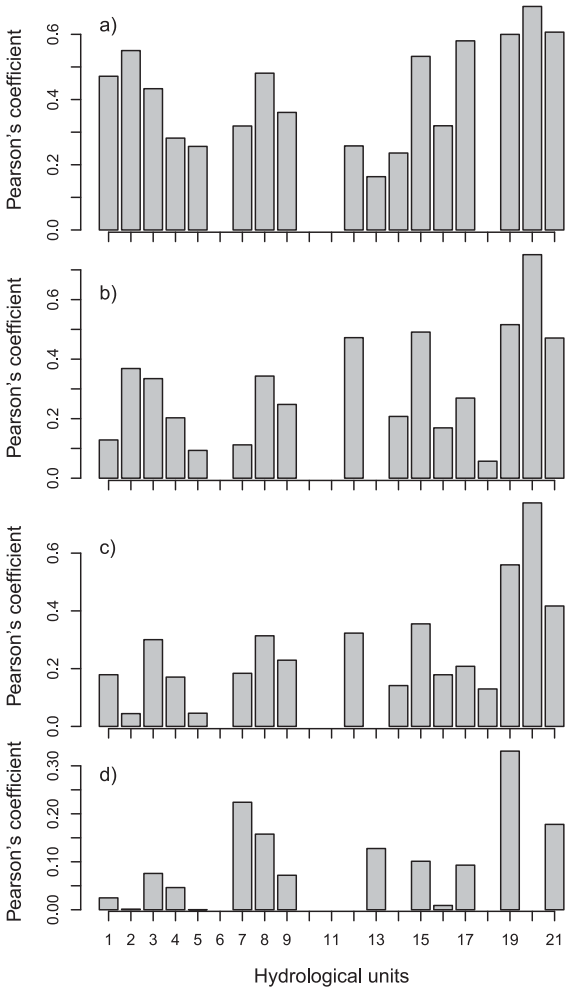

FIG. 16. Pearson's correlation between catchment-averaged hydrological rainfall characteristics and observations. (a) Seasonal rainfall total, (b) 99th percentile of daily rainfall, (c) 99th percentile of 3-day rainfall total, and (d) max number of consecutive wet days ($>1.0\,\text{mm day}^{-1}$) for 1974–2010.

regionwide conditions associated with a maxima deficit of atmospheric moisture offshore of the southern coast of the PAEP. The identity of the dry–wet state 3 was more evasive to infer from the synoptic climate setting and it was elucidated from the mechanistic description embedded in the state occurrences progression. Episodic dry states alternate in the core wet season and they also occur in the onset and retreat of the rainy period.

In the second step, seasonal predictions from two GCMs were first evaluated on their skill to hindcast 28 December–May (1982–2010) seasonal accumulated totals over the PAEP. The ECHAM4.5 hindcast made using retrospective simulations and predictions of the seasonally averaged ensemble-mean rainfall were found to be more skillful than the CFSv2 hindcast. The ECHAM4.5 historical simulations and predictions were analyzed to build up a set of predictors based on canonical correlation analysis (CCA). A canonical variate that summarizes most of the large-scale physically relevant information from the ECHAM4.5 simulations was found as the best predictor regionwide. An attempt to build a predictor from the ECHAM4.5 predictions resulted in a canonical variate with a low predictive skill. The loss of skill of the GCM predictions seems a dearth in reproducing the thermally driven rainfall (SST-signed rainfall) as the first mode of rainfall variability. The ECHAM4.5 historical canonical variate, a synthetic series, delivered the optimal coupled mode between the GCM ensemble mean and the PAEP rainfall in its temporal and spatial components. In the former, the signal-to-noise ratio was modulated to represent modes of variability during the non–El Niño and normal years. In the latter, GCM modes were retained that explained the rainfall variability at the regional level. A comparison of the spatial structures of these modes agrees with the atmospheric conditions influencing the wet weather states diagnosed by the HMM. Hence, this canonical variate was used as a predictor in the GCM–NHMM approach to generate an ensemble of 100 stochastic multisite realizations.

In terms of downscaling, the GCM–NHMM approach was able to reasonably capture the natural variability of the December–May accumulated total rainfall, mean intensity of wet days, and to a lesser extent the daily rainfall occurrences at regional level. A comparison with a CCA-based downscaling showed that the NHMM does not fully recover the predictive value of the input variable for the rainfall statistics of interest. Thus, the NHMM provides only moderate benefits compared to a CCA regression model when looking at seasonal accumulated time windows. However, at catchment level, the NHMM was able to convey most of the GCMs' large-scale simulation skill to daily rainfall characteristics relevant for hydrology in the southern catchments, with the seasonal rainfall total at the forefront, followed by extreme daily rainfall statistics. The NHMM skills decreased for the maximum number of consecutive wet days ($>1.0\,\text{mm day}^{-1}$). Overall, the NHMM overestimates the frequency of wet days per season during almost the entire hindcast period. The latter appeared to be related to the spatial correlation model used in the NHMM. The spatial model used assumes that rainfall stations are conditional independent of each other, given the rainfall state. Even though we describe the wet properties of the PAEP rainfall in terms of physically interpretable weather states, these weather states cannot entirely capture the complex spatial dependences of rainfall occurrences over high-elevation stations. In reality, sharp topographic gradients may impose high

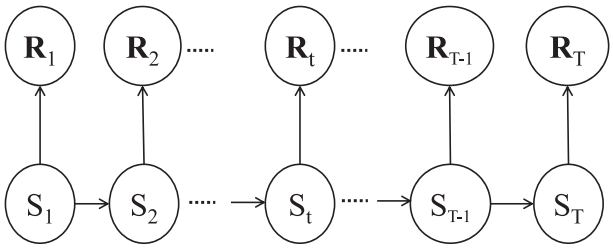

FIG. A1. Graphical model representation of an HMM.

spatial correlation between nearby stations. These high cross correlations in the extreme tails of the joint distribution are not explicitly accounted for by the NHMM. The investigation of a more suitable spatial model for the high regions is the subject of future work.

Acknowledgments. L. Pineda was funded by an EMECW grant of the European Commission for doctoral studies at KU Leuven. The authors thank A. Robertson for helpful comments and M. Bell for assistance with data processing, both from the IRI of Columbia University. The station data were provided by the National Services of Meteorology and Hydrology of Ecuador (INAMHI) and Peru (SENAMHI). The HMM and CPT tools used in this work were downloaded from the IRI website (http://iri.columbia.edu/our-expertise/climate/tools/).

APPENDIX

The HMM Structure and Assumptions

Let $\mathbf{R}_t = R_t^1, \ldots, R_t^M$ be a multivariate random vector of rainfall occurrences R over a network of M rain stations and let S_t be the hidden rainfall state of day t ($t = 1, \ldots, k$). The HMM factorizes the joint distribution of historical rainfall amount over a network of stations in terms of a few discrete states, by making two conditional assumptions. It is first assumed that the rainfall on a given day depends only on the states active on that day:

$$p(\mathbf{R}_t \mid S_{1:t}, R_{1:t-1}) = p(\mathbf{R}_t \mid S_t). \tag{A1}$$

The second assumption is that the state active on a given day depends only on the previous day's state,

$$p(S_t \mid S_{1:t-1}) = p(S_t \mid S_{t-1}), \tag{A2}$$

and that this first-order Markov process is homogeneous in time, that is, the $K \times K$ transition probability matrix for Eq. (A2) does not change in time. The conditional independence assumptions are easily visualized as edges in a directed graph of the HMM (Fig. A1).

For $p(\mathbf{R}_t \mid S_t)$, we make the simplifying assumption that the rainfall observation $\mathbf{r}$ at each station at time t is independent from observations at other stations at time t, conditional on the hidden state:

$$p(\mathbf{R}_t = \mathbf{r} \mid S_t = i) = \prod_{m=1}^{M} p(R_t^m = r \mid S_t = i) = \prod_{m=1}^{M} p_{imr}. \tag{A3}$$

This conditional independence assumption given the states does not imply spatial independence of the rainfall process. Spatial dependence is captured implicitly via the state variable.

REFERENCES

Barnston, A. G., and H. M. van den Dool, 1993: A degeneracy in cross-validated skill in regression-based forecasts. *J. Climate*, **6**, 963–977, doi:10.1175/1520-0442(1993)006<0963:ADICVS>2.0.CO;2.

——, Y. He, and M. H. Glantz, 1999: Predictive skill of statistical and dynamical climate models in SST forecasts during the 1997–98 El Niño episode and the 1998 La Niña onset. *Bull. Amer. Meteor. Soc.*, **80**, 217–243, doi:10.1175/1520-0477(1999)080<0217:PSOSAD>2.0.CO;2.

——, S. Li, S. J. Mason, D. G. DeWitt, L. Goddard, and X. Gong, 2010: Verification of the first 11 years of IRI's seasonal climate forecasts. *J. Appl. Meteor. Climatol*, **49**, 493–520, doi:10.1175/2009JAMC2325.1.

Bendix, J., 2000: Precipitation dynamics in Ecuador and northern Peru during the 1991/92 El Niño: A remote sensing perspective. *Int. J. Remote Sens.*, **21**, 533–548, doi:10.1080/014311600210731.

——, and W. Lauer, 1992: Rainy seasons of Ecuador and their climate-dynamic interpretation. *Erdkunde*, **46**, 118–134, doi:10.3112/erdkunde.1992.02.04.

Borbor-Cordova, M., E. Boyer, W. McDowell, and C. Hall, 2006: Nitrogen and phosphorus budgets for a tropical watershed impacted by agricultural land use: Guayas, Ecuador. *Biogeochemistry*, **79**, 135–161, doi:10.1007/s10533-006-9009-7.

Dempster, A. P., N. M. Laird, and D. R. Rubin, 1977: Maximum likelihood from incomplete data via the EM algorithm. *J. Roy. Stat. Soc.*, **39B** (1), 1–38.

Emck, P., 2007: A climatology of south Ecuador. Ph.D. thesis, Universität Erlangen, Erlangen, Germany.

Forney, G. D., Jr., 1973: The Viterbi algorithm. *Proc. IEEE*, **61**, 268–278, doi:10.1109/PROC.1973.9030.

Fu, G., S. Charles, F. Chiew, J. Teng, H. Zheng, A. Frost, W. Liu, and S. Kirshner, 2013: Modelling runoff with statistically downscaled daily site, gridded and catchment rainfall series. *J. Hydrol.*, **492**, 254–265, doi:10.1016/j.jhydrol.2013.03.041.

Ghahramani, Z., 2001: An introduction to hidden Markov models and Bayesian networks. *Int. J. Pattern Recognit. Artif. Intell.*, **15**, 9–42, doi:10.1142/S0218001401000836.

Goddard, L., A. G. Barnston, and S. J. Mason, 2003: Evaluation of the IRI's "net assessment" seasonal climate forecasts: 1997–2001. *Bull. Amer. Meteor. Soc.*, **84**, 1761–1781, doi:10.1175/BAMS-84-12-1761.

Greene, A. M., A. W. Robertson, and S. Kirshner, 2008: Analysis of Indian monsoon daily rainfall on subseasonal to multidecadal

time scales using a hidden Markov model. *Quart. J. Roy. Meteor. Soc.*, **134**, 875–887, doi:10.1002/qj.254.

——, ——, P. Smyth, and S. Triglia, 2011: Downscaling projections of Indian monsoon rainfall using a non-homogeneous hidden Markov model. *Quart. J. Roy. Meteor. Soc.*, **137**, 347–359, doi:10.1002/qj.788.

Hughes, J. P., and P. Guttorp, 1994: A class of stochastic models for relating synoptic atmospheric patterns to regional hydrologic phenomena. *Water Resour. Res.*, **30**, 1535–1546, doi:10.1029/93WR02983.

Kalnay, E., and Coauthors, 1996: The NCEP/NCAR 40-Year Reanalysis Project. *Bull. Amer. Meteor. Soc.*, **77**, 437–471, doi:10.1175/1520-0477(1996)077<0437:TNYRP>2.0.CO;2.

Lettenmaier, D. P., 1994: Applications of stochastic modeling in climate change impact assessment. *Stochastic and Statistical Methods in Hydrology and Environmental Engineering*, Vol. 3, K. W. Hipel et al., Eds., Kluwer Academic Publishers, 3–17.

Li, S., and L. Goddard, 2005: Retrospective forecasts with the ECHAM4.5 AGCM. IRI Tech. Rep. 05-02.

Muñoz, Á. G., and Coauthors, 2010: An environmental watch system for the Andean countries: El Observatorio Andino. *Bull. Amer. Meteor. Soc.*, **91**, 1645–1652, doi:10.1175/2010BAMS2958.1.

Ochoa, A., L. Pineda, P. Crespo, and P. Willems, 2014: Evaluation of TRMM 3B42 precipitation estimates and WRF retrospective precipitation simulation over the Pacific–Andean region of Ecuador and Peru. *Hydrol. Earth Syst. Sci.*, **18**, 3179–3193, doi:10.5194/hess-18-3179-2014.

Pineda, L., V. Ntegeka, and P. Willems, 2013: Rainfall variability related to sea surface temperature anomalies in a Pacific–Andean basin into Ecuador and Peru. *Adv. Geosci.*, **33**, 53–62, doi:10.5194/adgeo-33-53-2013.

Recalde-Coronel, G. C., A. G. Barnston, and A. G. Muñoz, 2014: Predictability of December–April rainfall in coastal and Andean Ecuador. *J. Appl. Meteor. Climatol.*, **53**, 1471–1493, doi:10.1175/JAMC-D-13-0133.1.

Robertson, A. W., S. Kirshner, and P. J. Smyth, 2004: Downscaling of daily rainfall occurrence over northeast Brazil using a hidden Markov model. *J. Climate*, **17**, 4407–4424, doi:10.1175/JCLI-3216.1.

——, ——, ——, S. P. Charles, and B. C. Bates, 2006: Subseasonal-to-interdecadal variability of the Australian monsoon over north Queensland. *Quart. J. Roy. Meteor. Soc.*, **132**, 519–542, doi:10.1256/qj.05.75.

——, V. Moron, and Y. Swarinoto, 2009: Seasonal predictability of daily rainfall statistics over Indramayu district, Indonesia. *Int. J. Climatol.*, **29**, 1449–1462, doi:10.1002/joc.1816.

Roeckner, E. K., and Coauthors, 1996: The atmospheric general circulation model ECHAM-4: Model description and simulation of present day climate. Max-Planck Institute for Meteorology Tech. Rep. 218, 90 pp. [Available online at http://www.mpimet.mpg.de/fileadmin/publikationen/Reports/MPI-Report_218.pdf.]

Rossel, F., and E. Cadier, 2009: El Niño and prediction of anomalous monthly rainfalls in Ecuador. *Hydrol. Processes*, **23**, 3253–3260, doi:10.1002/hyp.7401.

Saha, S., and Coauthors, 2006: The NCEP Climate Forecast System. *J. Climate*, **19**, 3483–3517, doi:10.1175/JCLI3812.1.

——, and Coauthors, 2014: The NCEP Climate Forecast System version 2. *J. Climate*, **27**, 2185–2208, doi:10.1175/JCLI-D-12-00823.1.

Schwarz, G., 1978: Estimating the dimension of a model. *Ann. Stat.*, **6**, 461–464, doi:10.1214/aos/1176344136.

Smith, T. M., R. W. Reynolds, T. C. Peterson, and J. Lawrimore, 2008: Improvements to NOAA's historical merged land–ocean surface temperature analysis (1880–2006). *J. Climate*, **21**, 2283–2296, doi:10.1175/2007JCLI2100.1.

Takahashi, K., 2004: The atmospheric circulation associated with extreme rainfall events in Piura, Peru, during the 1997–1998 and 2002 El Niño events. *Ann. Geophys.*, **22**, 3917–3926, doi:10.5194/angeo-22-3917-2004.

——, R. Martínez, A. Montecinos, B. Dewitte, D. Gutiérrez, and E. Rodriguez-Rubio, 2014: Regional applications of observations in the eastern Pacific: Western South America. *Proc. Tropical Pacific Observing System 2020 Workshop*, La Jolla, CA, WMO and Intergovernmental Oceanographic Commission, TPOS White Paper 8a. [Available online at http://www.wmo.int/pages/prog/gcos/Publications/gcos-184_II.pdf.]

Taylor, K. E., 2001: Summarizing multiple aspects of model performance in a single diagram. *J. Geophys. Res.*, **106**, 7183–7192, doi:10.1029/2000JD900719.

Tippett, M. K., M. Barlow, and B. Lyon, 2003: Statistical correction of central Asia winter precipitation simulations. *Int. J. Climatol.*, **23**, 1421–1433, doi:10.1002/joc.947.

Verbist, K., A. W. Robertson, W. M. Cornelis, and D. Gabriels, 2010: Seasonal predictability of daily rainfall characteristics in central northern Chile for dry-land management. *J. Appl. Meteor. Climatol.*, **49**, 1938–1955, doi:10.1175/2010JAMC2372.1.

Vuille, M., R. S. Bradley, and F. Keimig, 2000: Climate variability in the Andes of Ecuador and its relation to tropical Pacific and Atlantic sea surface temperature anomalies. *J. Climate*, **13**, 2520–2535, doi:10.1175/1520-0442(2000)013<2520:CVITAO>2.0.CO;2.

Wilks, D. S., 2006: *Statistical Methods in the Atmospheric Sciences*. 2nd ed. Academic Press, 627 pp.